Respiratory Physiology & Neurobiology 166 (2009) 142–151

Contents lists available at ScienceDirect

Respiratory Physiology & Neurobiology

journal homepage: www.elsevier.com/locate/resphysiol

Comparison of micron- and nanoparticle deposition patterns in a realistic human nasal cavity

S.M. Wang[a,b], K. Inthavong[b], J. Wen[a,b,*], J.Y. Tu[b,*], C.L. Xue[c]

[a] School of Energy and Power Engineering, Xi'an Jiaotong University, 710049, China
[b] School of Aerospace, Mechanical and Manufacturing Engineering, RMIT University, Australia
[c] School of Medical Sciences, RMIT University, Australia

ARTICLE INFO

Article history:
Accepted 27 February 2009

Keywords:
Nanoparticle
Micronparticle
Nasal cavity
Deposition

ABSTRACT

Knowledge regarding particle deposition processes in the nasal cavity is important in aerosol therapy and inhalation toxicology applications. This paper presents a comparative study of the deposition of micron and submicron particles under different steady laminar flow rates using a Lagrangian approach. A computational model of a nasal cavity geometry was developed from CT scans and the simulation of the fluid and particle flow within the airway was performed using the commercial software GAMBIT and FLUENT. The air flow patterns in the nasal cavities and the detailed local deposition patterns of micron and submicron particles were presented and discussed. It was found that the majority of micron particles are deposited near the nasal valve region and some micron particles are deposited on the septum wall in the turbinate region. The deposition patterns of micron particles in the left cavity are different compared with that in the right one especially in the turbinate regions. In contrast, the deposition for nanoparticles shows a moderately even distribution of particles throughout the airway. Furthermore the particles releasing position obviously influences the local deposition patterns. The influence of the particle releasing position is mainly shown near the nasal valve region for micron particle deposition, while for submicron particles deposition, both the nasal valve and turbinate region are influenced. The results of the paper are valuable in aerosol therapy and inhalation toxicology.

1. Introduction

Nasal inhalation is a major route of entry into the body for airborne pollutants by which workers in occupational environments and the general population are exposed to. It was found that the limit for inhalable particles in calm air for nasal inhalation was 135 μm (Dai et al., 2006). This leads to a significant number of inhalable toxic particles, given that a large proportion of pollutants exist from the nanorange up to 50 μm in pollen (Harrington and Metzger, 1963). On the other hand, drug particles are deliberately sprayed into the nasal cavity in the event that the drug particles will deposit on the targeted sites for efficient drug delivery. Therefore the function of the nose to filter out toxic particles is a necessity however causes inefficiencies in drug delivery. Particles such as dusts, pollen and sprays that exist in the micron size range are generally visible and deposition by inertial impaction is common. Finer particles such as fumes, gases and smoke that exist in the submicron range are less visible exhibiting low Stokes numbers and deposition is considered to be diffusion dominant.

Knowledge regarding particle deposition processes in the nasal cavity is important in aerosol therapy and inhalation toxicology. Experimental studies into aerosol deposition in the nasal cavity have been investigated in the past by a number of researchers. Cheng et al. (1988) measured the total deposition of submicron aerosols (5–200 nm) in a nasal cast at constant flow rates between 4 and 50 L/min. The deposition efficiency increased with decreasing particle size and flow rate, indicating that diffusion was the dominant mechanism. Cheng et al. (1996) also measured submicron particles ranging from 4 to 150 nm at constant flow rates of 10 and 20 L/min. Other studies related to submicron particles for constant flow rates include, Swift et al. (1992) and Swift and Strong (1996). Kesavanathan and Swift (1998) studied the effects of micron sized particles, nostril shape and nasal geometry on the total deposition efficiency among 10 volunteers under constant flow rates of 15, 25 and 35 L/min. In all these studies, either micron or submicron particles were used exclusively and a comparison between the two types of particles were not performed. And the detailed local deposition patterns were not provided which is very important in the studies of aerosol therapy and inhalation toxicology.

* Corresponding authors.
E-mail addresses: jianwen@mail.xjtu.edu.cn (J. Wen), jiyuan.tu@rmit.edu.au (J.Y. Tu).

1569-9048/$ – see front matter © 2009 Elsevier B.V. All rights reserved.
doi:10.1016/j.resp.2009.02.014

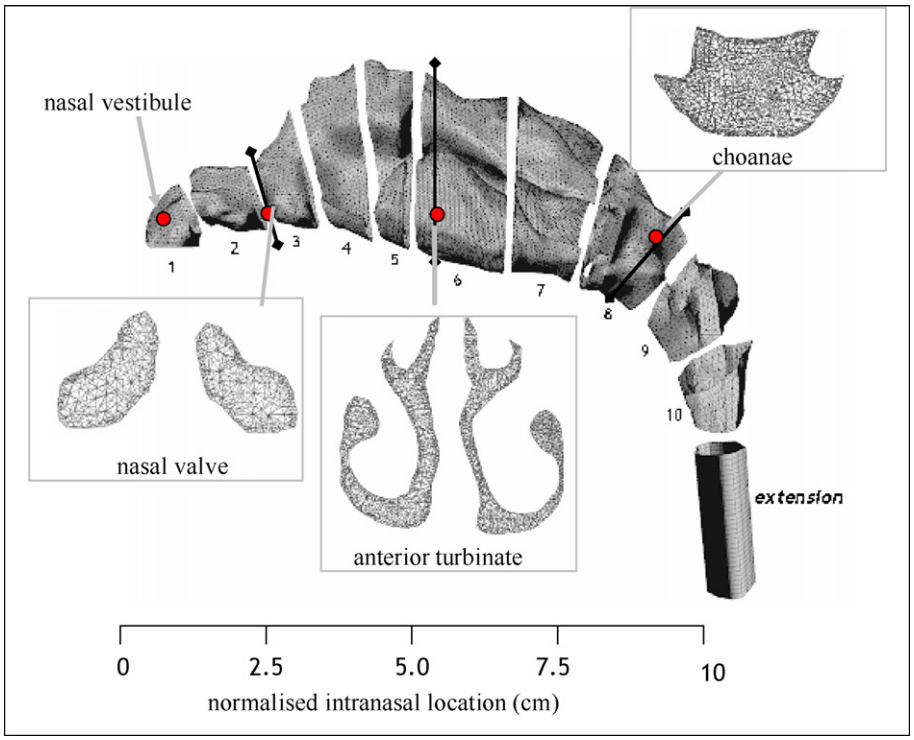

Fig. 1. Nasal cavity model used in the study which has been divided into 10 separate sections named (Zone 1–10) for analysis of local deposition. Cross-sectional areas taken at the nasal valve, middle turbinate and nasopharynx regions are shown with the computational mesh.

Experimental methods performed on human subjects are limited due to the invasive nature and dangers associated with toxic aerosols. The use of surrogate laboratory animals provide one alternative however the resultant data is often extrapolated due to the different airway dimensions and breathing characteristics. Computational simulations present another alternative to provide complementary data for difficult and expensive experimental studies. Yu et al. (1998) simulated nanospherical particles (1–10 nm) under a laminar constant flow rate of 15 L/min using an Eulerian approach. Zamankhan et al. (2006) simulated submicron particles in the range of 1–100 nm under different constant laminar flow rates between 4 and 14 L/min using a Lagrangian approach. The results showed that the deposition efficiency was a function of $Q^a D_{diff}^b$ where Q (L/min) is the flow rate and D_{diff} (cm^2/s) is the particle diffusion coefficient. The empirical constants 'a' and 'b' were tuned to fit the data sets. Shi et al. (2006) studied the transport and deposition of nanoparticles, i.e. 1–2 nm, under a transient laminar airflow. The study of micron particle deposition is not as notable in the literature. The deposition patterns for submicron and micron particles will inevitably be different due to the deposition mechanisms that each particle type experiences. Only Zhang et al. (2005) compared the deposition patterns of the two particle types but in the human upper airway that included the oral cavity, pharynx, larynx and trachea. The study made use of both the Eulerian and Lagrangian approaches for nanoparticles and micron particles, respectively, applied under constant flow rates of 15–60 L/min.

This paper presents a comparative study of the deposition of submicron particles, particularly the nanoparticles (1–10 μm) and micron particles under different steady laminar flow rates by using the Lagrangian approach. The significance and influence of different factors that are applicable to micron and nanoparticles are discussed and the detailed local deposition patterns presented. A comparison of the two groups of particle deposition patterns in the human nasal cavity is shown. The investigation in this paper was initiated due to the needs in health risk assessment on potentially toxic particles and the results are also applicable in targeted drug delivery with aerosols.

2. Nasal cavity geometry

A nasal cavity geometry was obtained through CT scans of the nose of a healthy 25 year old, Asian male, 170 cm height, 75 kg mass as shown in Fig. 1. The CT scan was performed using a CTI Whole Body Scanner (General Electric). The single-matrix scanner was used in helical mode with 1 mm collimation, a 40 cm field of view, 120 kV peak and 200 mA. The scans captured outlined slices in the X–Y plane at different positions along the Z-axis from the entrance of the nasal cavity to just anterior of the larynx at intervals of 1–5 mm depending on the complexity of the anatomy. The coronal sectioned scans were imported into a three-dimensional (3D) modelling program called GAMBIT (ANSYS Inc., USA) which created smooth curves that connected points on the coronal sections. Stitched surfaces were then created to form a complete computational mesh. Because the details of the flow velocity and pressure were not known prior to the solution of the flow problem, the outlet boundary condition was defined as an outflow with zero diffusion flux for all flow variables in the direction normal to the exit plane. This implies that the flow characteristics have to be consistent with a fully developed flow assumption and a straight extension of the outlet plane was created into the geometry to satisfy this criterion.

An initial model with 82,000 unstructured tetrahedral cells was initially used to solve the air flow field at a flow rate of 10 L/min. The model was then improved by cell adaptation techniques that included refining large volume cells, cells that displayed high velocity gradients and near wall refinements, where a model with a higher cell count was produced. This process was repeated twice, with each repeat producing a model with a higher cell count than the previous model. Subsequently four models were produced, 82,000, 586,000, 950,000 and 1.44 million cells. A grid independence test shown in Fig. 2, found the results for average velocity and

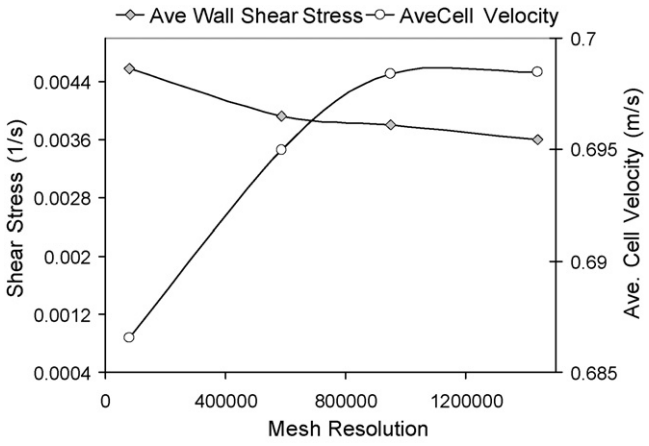

Fig. 2. Grid independence test based on the average cell velocity and shear stress values for the four different cavity models.

the wall shear stress converge as the mesh resolution approached 950,000 cells. In order to make a compromise between the result's accuracy and computational cost, a model with 950,000 elements was used in this study. The detailed numerical methods and procedure are shown in Appendix A.

3. Results and discussions

In this section, transport and deposition of micron and submicron size particles in the nasal airway are studied. Trajectories of small particles in the size range of 1 nm to 50 μm for different breathing rates were simulated using the Largrangian discrete phase analysis of the FLUENT code. To study the effect of particle size and breathing rate on the nasal capture efficiency, particles of a given size were injected uniformly at both nostrils. Particle trajectories were simulated and the corresponding capture efficiencies were evaluated. Regional deposition of different sized particles for different breathing rates was also studied, and the effects of particle density were analysed. To account for the stochastic process of Brownian motion, the capture efficiency for each particle group within the submicron range was calculated based on an average of 10 separate simulations.

For evaluating the particle deposition rates, the possibility of the particle rebounding from the passage surfaces was ignored and it was assumed that if the distance between the particle centre and the surface was less than or equal to the particle radius the particle will attach to the surface.

3.1. Model validation

3.1.1. Pressure drop

The average pressure drop between the nostril and nasopharynx was obtained at flow rates from 4 to 40 L/min (Fig. 3). At these flow rates, the corresponding range of Reynolds numbers at the inlets is 555–2424. A laminar model for the flow rates 4–15 L/min and the low Reynolds k–ω turbulent model for the flow rates 20–40 L/min were used to simulate the flow field. The model equations for the turbulent model are not given in this paper for brevity as the study's focus and results are based on flow rates between 4 and 15 L/min. The numerical results show good agreement with reported experimental data especially at flow rates less than 20 L/min. There is a slight discrepancy in the results for a flow rate of 40 L/min which may be attributed to some experimental uncertainties as well as inter-subject variability between the nasal cavity models where wider cross-sectional areas can produce less resistance to fluid flow and therefore less pressure drop.

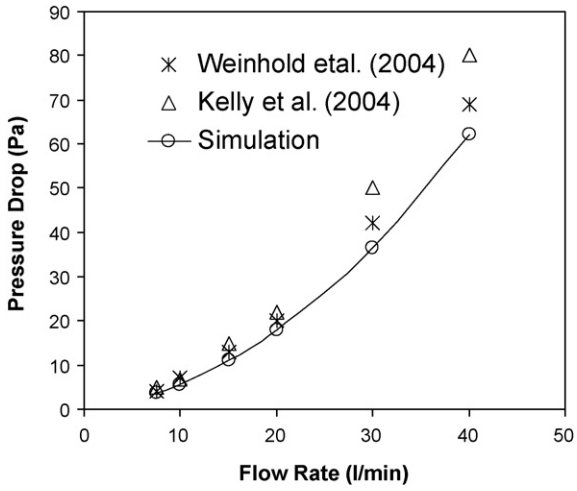

Fig. 3. Kelly et al., 2004; Pressure drop across the human nasal cavity as a function of inspiratory flow rate compared with reported experimental data.

3.1.2. Inertial deposition of particles

The inertial deposition of micron particles in the nasal cavity was normalised by using the inertial parameter:

$$I = Qd_{ae}^2 \quad (1)$$

where Q is the air flow rate and d_{ae} is the equivalent aerodynamic diameter. It is a convenient parameter that compares deposition against different flow rates and particle sizes at aerodynamic diameters. It is widely used for presenting particle deposition efficiencies, especially for in vivo data, where it is difficult to determine an adequate characteristic length for realistic human airways. Monodispersed particles in the range of 1–50 μm were released passively into the nasal cavity with flow rates between 4 and 14 L/min. The deposition of micron particles as a function of the inertial parameter is shown in Fig. 4. The simulated micron particle deposition in the present nasal cavity model was compared with experimental data that used other nasal cast models. Generally speaking, our computational data points show reasonable agreement with the experimental data.

Differences in deposition may be attributed to the inter-subject variability between the nasal cavity models, such as wider nasal replicate casts which can cause less deposition due to secondary flows (Häußermann et al., 2001). The neglect of the effect of sur-

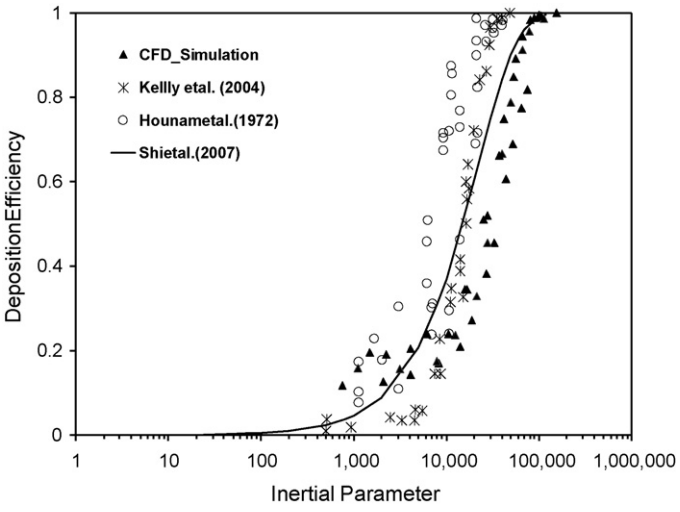

Fig. 4. CFD simulation results for total deposition of micron particles against inertial parameter compared with the experimental data.

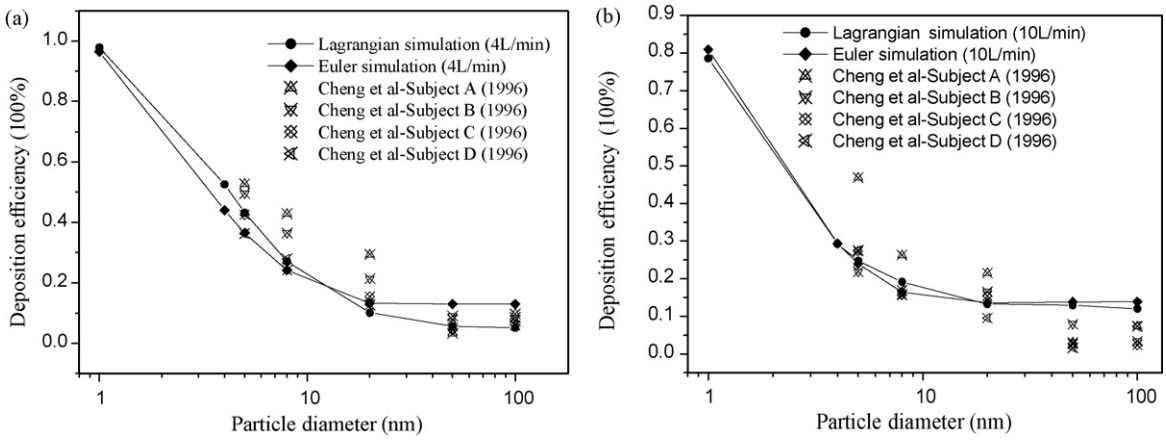

Fig. 5. Comparison between simulation and experimental data of nasal deposition efficiency for different nanoparticle size.

face roughness also caused the difference. Numerical geometry construction and subsequent mesh generation in computer simulations produced smooth wall surfaces, which may underestimate the inertial particle deposition efficiencies (Shi et al., 2007).

3.1.3. Diffusional deposition of submicron particles

The diffusional deposition of submicron particles (1–150 nm) was simulated under flow rates of 4 and 10 L/min (Fig. 5). Both the Eulerian and Lagrangian approaches for nanoparticles were presented in the figures. Comparisons of the simulated results were made with the available experimental data reported by Cheng et al. (1996) for nasal cavities with different anatomical features. Here the solid lines correspond to the model prediction. High deposition reaching 80% and nearly 100% were found for 1 nm particles at the corresponding flow rates of 4 and 10 L/min, respectively. High diffusional deposition is found for particles up to approximately 50 nm where particles that are larger provide little change in the total deposition. The deposition for 50 nm or larger particles is approximately 10% which is constant for both flow rates, suggesting that the flow rate has little effect on particles in the size range of 50–150 nm. The comparisons with the data of Cheng et al. (1996) show similar values. The numerical results of Lagrangian approach are more close to the experimental data compared with that of Eulerian approach under laminar conditions. Thus the Lagrangian approach was employed for nanoparticles in the paper. As discussed earlier differences in the results may be attributed to anatomical variances in the nasal cavities used.

In summary, the good agreements between published experimental data and simulated results instill confidence that the present simulation model is sufficiently accurate to analyse laminar fluid flow as well as micron and submicron particle deposition in the three-dimensional nasal cavity.

3.2. Air flow patterns

Flow streamlines were captured by tracking the path traversed by a massless particle released from the inlet of each cavity which provides a qualitative visualization of the flow field. Airflow patterns for the left nasal cavity at a flow rate of 7.5 L/min (Fig. 6a) show flow separation and reversed flow in the upper regions of the airway which is the location of the olfactory sensors, just posterior to the nasal valve. The horse-shoe shaped vortex is a result

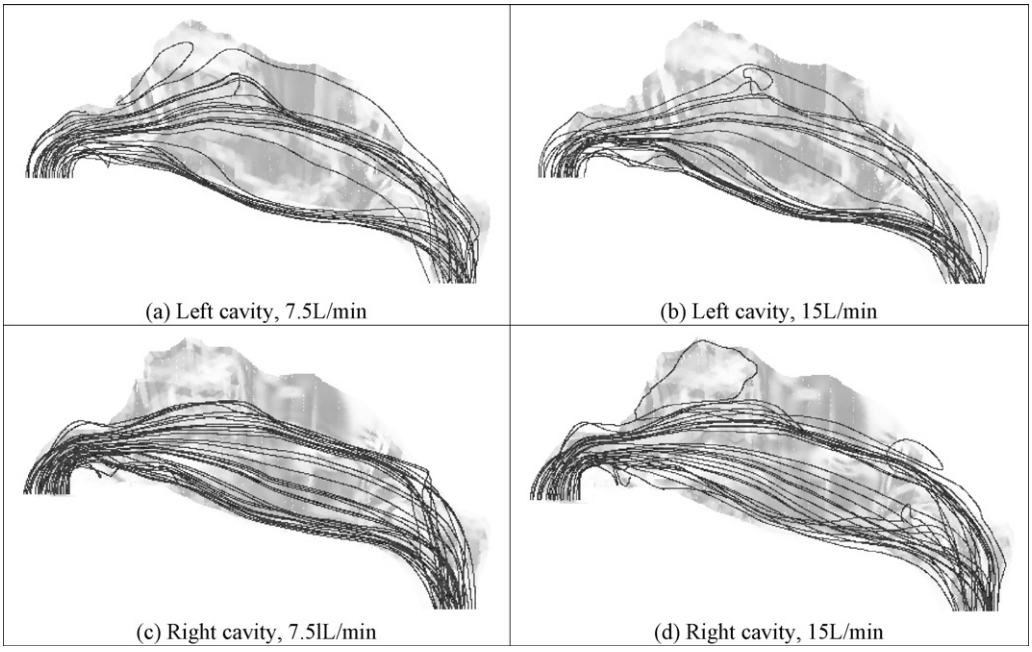

Fig. 6. Flow streamlines in the nasal cavity at different rate.

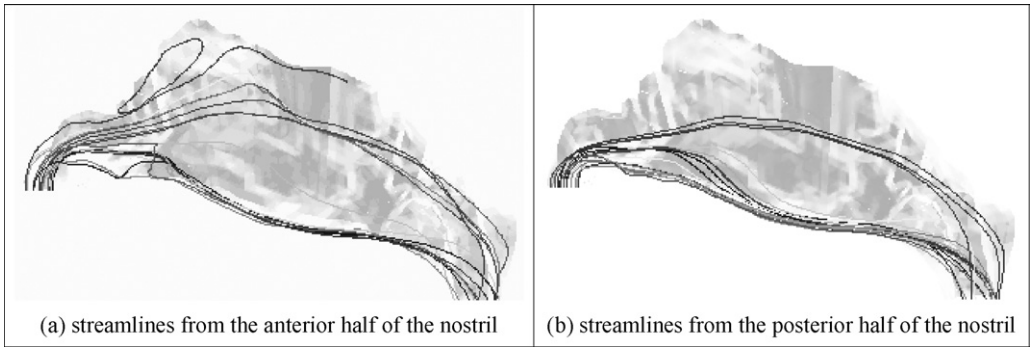

Fig. 7. Representation of flow streamlines in the left cavity at flow rate of 7.5 L/min.

of the adverse pressure gradient caused by the abrupt increase in cross-sectional area from the nasal valve to the main nasal passage. As the flow rate increases to 15 L/min (Fig. 6b), the vortex moved posteriorly to the middle region of turbinate and was smaller. The streamlines in the right cavity at a flow rate of 7.5 L/min (Fig. 6c), showed no recirculation and most of the streamlines are concentrated in the middle and lower regions of the nasal cavity. At a flow rate of 15 L/min (Fig. 6d), two vortices are found. The bigger vortex is just posterior to the nasal valve while the smaller vortex is found in the posterior turbinate region. These results demonstrate that the flow patterns in the nasal cavity are sensitive to the anatomic geometry and flow rate.

The streamlines from different injection locations are shown in Fig. 7. The flow streamlines released from the anterior half of nostrils go through the upper, middle and lower part of the cavity and most of them concentrated in the middle and lower part (Fig. 7a), while a majority of the streamlines released from the posterior half of nostrils only go through the floor of the airway and another proportion flows around the mid-height cavity (Fig. 7b). Because of a low-lying nasal roof, both the flow rising upward from the nostril was observed to bend towards the floor as well as laterally. The complex flow in this nasal valve region therefore acts as a filtration device for particle deposition—a fact that is positive for toxic inhalation but a problem for drug delivery.

3.3. The comparison of particle deposition patterns

3.3.1. Local deposition patterns

Local deposition patterns for micron submicron particles were studied. The discrete particles were tracked and the fate of each particle recorded. A particle was deemed deposited if its trajectory impacted onto the wall surfaces, otherwise the particle escaped through the outlet. The visualised deposition patterns of 22 μm and 1 nm particles with the density of 1000 kg/m^3 is shown in Fig. 8. For both of the left and right cavities, most of the submicron particles are deposited in the anterior and middle regions. The upper region of Zone 2 (defined in Fig. 1) is a 'hot spot' for deposition (Fig. 8a). This may be explained by the curvature in the nasal geometry that exhibits a 90° bend from the nostril inlet into the main nasal passage. The 22 μm particles that were initially entrained in the flow path at the inlet are not able to change its flow direction because of the particle inertia, which leads to impaction in the upper region of Zone 2. The inertial impaction caused by the 90° bend is found again in the posterior region of the nasal cavity where the flow changes direction from the main nasal passage towards the larynx. Other local deposition sites are found in the upper regions of the middle sections at Zones 4, 5 and 6 for left cavity (Fig. 8b) and at Zone 3 and 6 for right cavity (Fig. 8c). The flow field forces the particles to remain close to the septum walls and is pushed in an upward direction where the local deposition sites are found. A small hot spot for

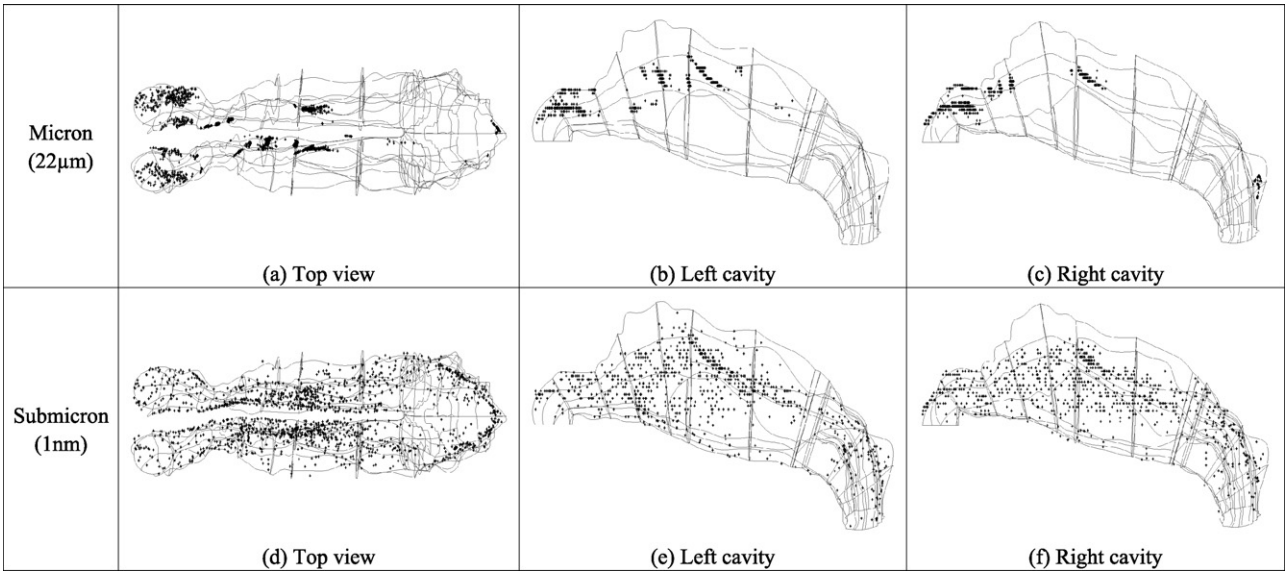

Fig. 8. Local deposition patterns of particles released uniformly from the nostrils for a flow rate of 10 L/min. (Micron particle having a density 1000 kg/m^3 and a diameter of 22 μm. Nanoparticle having a density 1000 kg/m^3 and a diameter of 1 nm. Both particles exhibit the same deposition efficiency of 80%.)

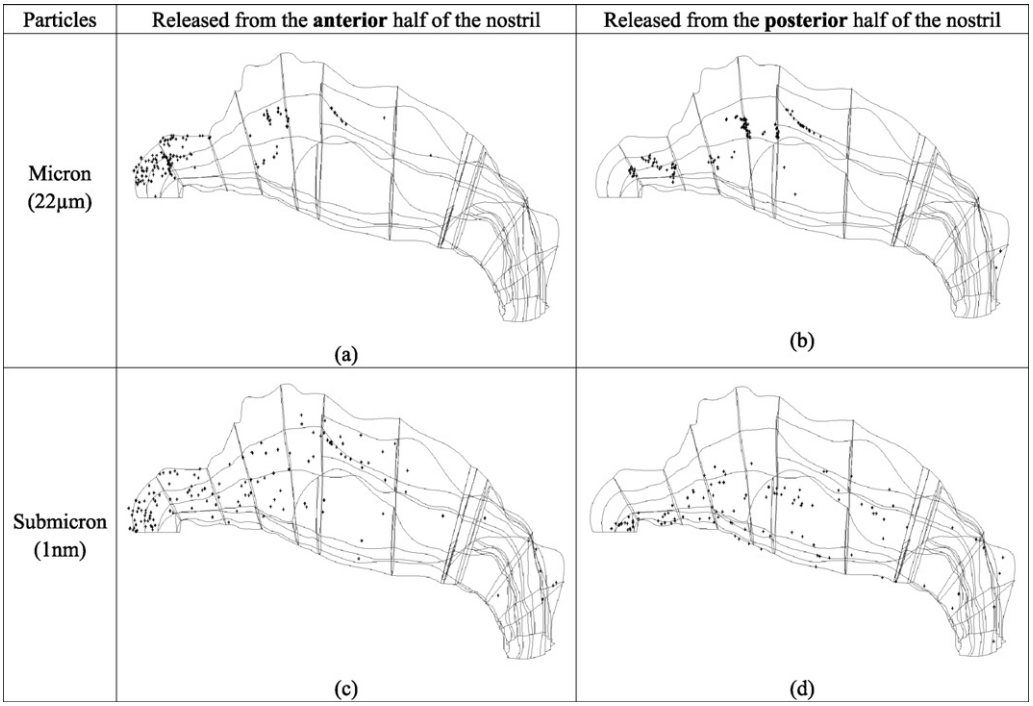

Fig. 9. Local deposition patterns of particles released uniformly from the different part of the left nostril for a flow rate of 10 L/min. (Micron particle having a density 1000 kg/m^3 and a diameter of 22 μm. Nanoparticle having a density 1000 kg/m^3 and a diameter of 1 nm. Both particles exhibit the same deposition efficiency of 80%.)

deposition is found near the right nasopharynx (Fig. 8c). The deposition of 22 μm particles is dominant in the anterior regions and this region is characterized by the convergent–divergent shape of the nasal valve. The left cavity shows greater deposition than right cavity especially in the middle region. The results demonstrate that the geometry morphology is a non-ignorable factor in the micron particle deposition. The deposition pattern for a 1 nm particle with the density of 1000 kg/m^3 shows a vastly different deposition pattern when compared with the 22 μm particle, although the total deposition efficiency is the same (80%) for both particles. The deposited nanoparticles are distributed more evenly, not only in the entire nasal cavity, but also within each zone (Fig. 8d). There is not much difference in the left and right nasal cavities (Fig. 8e and f). The diffusion mechanism of deposition for 1 nm particles disperses the particles in all directions.

The local deposition patterns of particles released from different part of the left nostril are shown in Fig. 9. There is not much difference for micron particle deposition except near the nasal valve region for the airflow separation mentioned in the former section (Fig. 9a and b). For nanoparticle deposition, the difference caused by the particles releasing position is obvious. The particles released from the anterior half nostril are deposited mainly in the upper valve and the middle and upper nasal turbinate regions (Fig. 9c), while the particles released from the posterior half nostril are mainly deposited in the lower valve and the middle and lower nasal turbinate regions (Fig. 9c). The above results can provide data that is pertinent to the prediction of gas-particle flows and also regional tissue exposure to inhaled air that are found in toxicology and therapeutic inhalation studies.

The total deposition in the entire nasal cavity is quantified in terms of the total deposition efficiency (*TDE*) as:

$$TDE = \frac{\text{number of deposited particles in nasal cavity}}{\text{number of particles entering the nasal cavity}} \quad (2)$$

The local deposition efficiency (*LDE*) is calculated for each of the 10 subdivided zones presented in Fig. 1. For better comparisons between the different zones, the *LDE* takes into account the zone surface area since the each zone exhibits different sizes.

$$LDE = \frac{\text{number of deposited particles in local region}/\text{number of deposited particles in nasal cavity}}{A_{\text{zone}}/A_{\text{total}}} \quad (3)$$

Fig. 10 shows the deposition fraction in each zone for the two particle types. The *LDE* normalised by the zone's surface area shows a high concentration of particle deposition for 22 μm particles in Zone 2. Before normalisation, the deposition efficiency for Zone 6 was found to contribute 32% of the total deposition. However because of the larger surface area the normalised *LDE* in figure shows a smaller concentration of deposited particles per area. Besides the high concentration of deposited particles in Zone 2, the spread of deposited particles among the other zones are generally even, except for Zones 7 and 8 which have very little deposition.

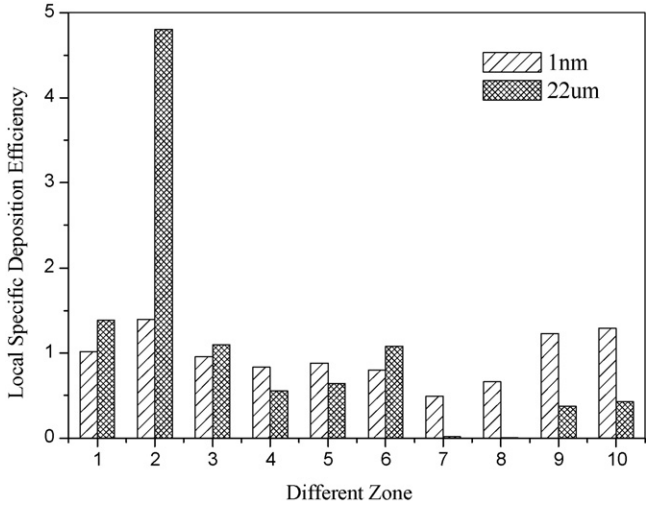

Fig. 10. Deposition patterns of 1 nm and 22 μm at inspiratory flow rate of 10 L/min (density = 1000 kg/m^3, total deposition efficiency = 80%).

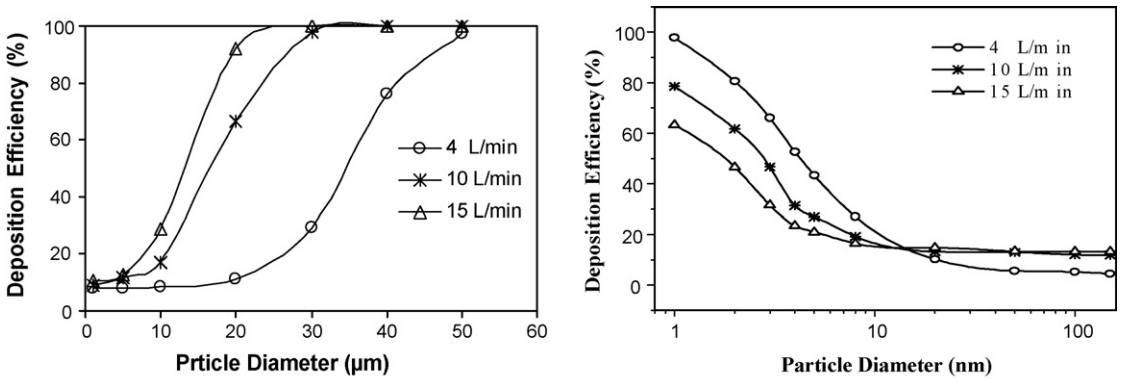

(a) micron particles with the density of 1000 kg/m³ (b) nano particles with the density of 1000kg/m³

Fig. 11. Simulated deposition efficiency as function of diameter using different inspiratory flow rate.

In comparison the deposition pattern for the 1 nm particle shows a uniformly distribution of particle deposition.

3.3.2. Effect of flow rate and density

Fig. 11a plots the total deposition efficiency for micron particles with the density of 1000 kg/m^3 as a function of particle size for three inspiratory flow rates. For flow rates ranging from 4 to 15 L/min, the deposition efficiency increases nonlinearly with the diameter where micron particles smaller than 10 μm exhibit low deposition efficiencies (<15%). However, the deposition efficiency rises rapidly when the diameter is larger than 20 μm. The deposition efficiency increases from 21.0% of 20 μm to 93.2% of 50 μm at 7.5 L/min. For a given micron particle, the deposition efficiency also increases significantly with the increase in the flow rate. For 20 and 30 μm particles, the deposition efficiencies increase by 35.4% and 42.4%, respectively when flow rate increases from 7.5 to 15 L/min.

Fig. 11b shows the deposition efficiencies for submicron particles with a density of 1000 kg/m^3 as a function of particle diameter at different flow rates. The deposition efficiencies of nanoparticles decrease with particle size. The three curves for different flow rates converge when the particle size approaches 15 nm. The deposition efficiency decreases as the particles increase in size from 1 to 15 nm. For particles larger than 15 nm and up to 100 nm, only a slight decrease is observed in the deposition efficiency. This result may suggest that the 15 nm particle size is a critical value for distinguishing the type of deposition that is involved, where the effects of diffusion becomes less prominent as the particles increase in size. The effects of the flow rate show that an increase in the flow rate decreases the deposition efficiency which is quite different in comparison with micron particles. The higher flow rates produce only slightly larger deposition efficiencies than that for lower flow rates.

In particle deposition studies, the Stokes number (St) given by:

$$St = \frac{\rho_p d_p^2}{18\mu_g}\frac{U}{D} \tag{4}$$

is a ratio of the relaxation time, $\tau = \rho_p d_p^2/18\mu_g$ to the particle's characteristic time U/D, where U is the air phase system characteristic velocity normally taken as the air phase inlet value and D is the characteristic length. It can be used to normalise the effects of the particle density, diameter and the corresponding flow rate. The Stokes number is significantly influenced by the particle diameter, while the effect of density is linearly related. For micron particles that exist in orders of scales similar to μ_g and U/D, the effects of inertia and therefore density are somewhat important. For submicron particles the particle diameters are three scales smaller than microns and the particle relaxation time, τ becomes very small. Additionally particle diffusion is dominant for nanoparticles and the effects of the flow rate on the deposition are found to be secondary while changes caused by density are negligible (Table 1). In experimental studies normalisation for inertial particle deposition is by Eq. (1) (the inertial parameter) while for diffusion dominant particle deposition normalisation is performed by the parameter $Q^a D_{diff}^b$ (Cheng et al., 1988; Swift et al., 1992), where Q (L/min) is the flow rate and D_{diff} (cm^2/s) is the particle diffusion coefficient. The superscripts a and b are empirically defined constants. Clearly the main difference in the normalisation between micron particles to submicron particles is the particle density which has an effect

Table 1
Deposition efficiency (%) of different densities for (a) micron particles (10 L/min) and nanoparticles (10 L/min).

(a)					
Diameter (μm)	100 (kg/m^3)	500 (kg/m^3)	1000 (kg/m^3)	1500 (kg/m^3)	2000 (kg/m^3)
1	8.5	9.3	9.3	9.6	10.3
5	9.8	11.1	11.8	12.5	13.5
10	10.8	13.0	17.2	26.4	36.0
20	13.2	33.4	66.5	89.8	97.2
50	42.1	99.8	100	100	100
(b)					
Diameter (nm)	100 (kg/m^3)	500 (kg/m^3)	1000 (kg/m^3)	1500 (kg/m^3)	2000 (kg/m^3)
1	78.1	78.4	77.7	79.3	79.3
5	25.1	25.2	24.9	24.7	24.5
8	19.2	19.17	19.19	19.21	19.15
20	13.3	13.27	13.25	13.28	13.26
50	12.88	12.9	12.91	12.92	12.86

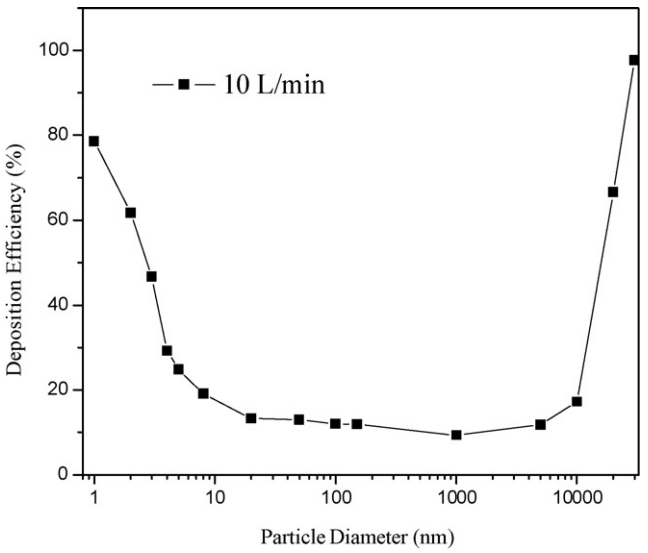

Fig. 12. Variations of particle deposition fractions vs. particle size in the nasal cavity at the inspiratory flow rate of 10 L/min.

on the inertial impacting micron particles but is insignificant for submicron particles.

3.3.3. Comparison of deposition mechanism

It was shown that particle deposition in the nasal cavity is effected by particle size, flow rate and sometimes density. There are four mechanisms of deposition that cause particle deposition in the human nasal cavity: inertial impaction, sedimentation, diffusion and interception. Interception is similar to impaction and occurs when a particle touches a surface. Interception is a more important deposition mechanism for fibres than for spherical particles as the length and particle orientation relative to flow streamlines are meaningless for spherical particles, but of central importance to fibres. Therefore Fig. 12 which does not account for interception due to the nature of Lagrangian point tracking shows the deposition efficiency over the range of 1–10,000 nm or 1 nm to 10 μm. Inertial impaction is the primary deposition mechanism for particles having a diameter greater than 1000 nm (1 μm). Due to the geometry in the nasal cavity the air enters the nostrils vertically before changing directions 90° towards the main nasal passage. Micron particles that have sufficiently high momentum will maintain their original linear path and impact on the nasal walls instead of following the curving streamlines. For particles <50 nm the rate of diffusion is inversely proportional to particle size, making the deposition mechanism diffusion dominant. Brownian motion is caused by collision of small particles by air molecules in the nasal cavity, and concentration gradients result in particle movement towards the nasal wall. Particles with a diameter in the size range of 0.05–1 μm have similar deposition efficiencies. For this particle range, all three deposition mechanisms, diffusion, inertial impaction and sedimentation have an effect albeit on a smaller scale.

4. Conclusion

A comparative study of the deposition of submicron particles and micron particles under different steady laminar flow rates using the Lagrangian approach was presented. The significance and influence of different factors that are applicable to micron and submicron particles were discussed and the detailed local deposition patterns were presented. It was found that the particle diameter has substantial influence on deposition patterns for both the micron particles and submicron particles. The total deposition efficiency of the micron particles increase as the particle diameter increases, while the inverse is true for submicron particles. The inspiratory flow rate also has some effect on the particle deposition. For micron particles, the total deposition efficiency increases with an increase in the flow rate. For nanoparticles less than 15 nm however, the efficiency decreases as the increase of flow rate. The particle density is only significant for micron particles in its contribution to the particle inertia. Overall there is a difference in the local deposition patterns for micron and submicron particles. The major regions of deposition for micron particles were found to be at the nasal valve and the middle septum parts in the nasal turbinate and there is some difference in left and right cavities, while for submicron particles there was a uniform distribution of deposited particles. Particle releasing position also has effect on the particle deposition. The influence of the particle releasing position is mainly shown near the nasal valve region for micron particle deposition, while for submicron particles deposition, both the nasal valve and turbinate region are influenced. The results can provide data that is pertinent to the prediction of gas-particle flows and also regional tissue exposure to inhaled air that are found in toxicology and therapeutic inhalation studies.

Acknowledgements

The paper is supported by the Australian Research Council (Project ID LP0561870), the National Natural Science Foundation of China (50676074) and the Principal Foundation of XJTU, for which the authors are thankful.

Appendix A

A.1. Governing equations

Due to the complex geometry of the anatomically real nasal cavity a commercial CFD code, FLUENT 6.3, was used to predict the continuum gas phase flow under steady-state conditions through solutions of the conservation equations of mass and momentum. These equations were discretised using the finite volume approach. The third order accurate QUICK scheme was used to approximate the momentum equation while the pressure–velocity coupling was resolved through the SIMPLE method. Flow rates ranging from 4 to 15 L/min were used. At these flow rates, the flow regime has been determined to be laminar (Hahn et al., 1993; Kelly et al., 2000; Swift and Proctor, 1977; Zamankhan et al., 2006; Wen et al., 2008). A steady flow rather than a cyclic unsteady flow was used in this case to focus on the parameters that govern the particle trajectories of micron and submicron particles independent from cyclic conditions. Moreover the significance of the fluctuating sinusoidal pattern of the inhalation–exhalation breathing cycle on the nasal airflow can be estimated by examining the Womersley number, α and the Strouhal number, S. The calculated Womersley number:

$$\alpha = \frac{D}{2}\left(\frac{\omega}{\nu_g}\right)^{0.5} \tag{A1}$$

was 1.68 while the Strouhal number:

$$S = \frac{\omega D}{u_{ave}} \tag{A2}$$

was 0.01. D is equal to 0.01 m and is the characteristic length which was taken as the average hydraulic diameter of 30 cross-sections taken throughout the nasal cavity. ν_g is the kinematic viscosity of air and ω is the breathing frequency equal to $\omega = 2\pi f = 1.57\ s^{-1}$ and u_{ave} is the average velocity through the nasal passage under the flow rate of 15 L/min which is equal to 0.9 m/s. Although the Womersley number is greater than 1, it is not much greater, while the low value

for S suggests that the flow may be assumed to be quasi-steady. It has however, been shown experimentally that the oscillatory effects are not present until $\alpha \to 4$ (Isabey and Chang, 1981). Additionally studies have also concluded that under most conditions especially low flow rates, the nasal airflow can be considered quasi-steady (Chang, 1989; Hahn et al., 1993; Sullivan and Chang, 1991). The steady-state continuity and momentum equations for the gas phase (air) in Cartesian tensor notation are:

$$\frac{\partial}{\partial x_i}(\rho_g u_i^g) = 0 \tag{A3}$$

$$u_j^g \frac{\partial u_i^g}{\partial x_j} = -\frac{1}{\rho}\frac{\partial p_g}{\partial x_i} + \frac{\partial}{\partial x_j}\left(\nu_g \frac{\partial u_i^g}{\partial x_j}\right) \tag{A4}$$

where u_i^g is the i-th component of the time averaged velocity vector and ρ_g is the air density. For the boundary conditions, a no slip flow velocity on the passage surfaces was assumed. At the nostril, a uniform flow perpendicular to the inlet was specified. Keyhani et al. (1995) specified the velocity profile at the nostril based on experimental data which showed that for a given flow rate, the downstream flow field is not significantly affected by the details of the velocity profile at the nostril. At the outlet a straight extension was created to allow for an outflow Neumann-type boundary condition:

$$\frac{\partial \phi}{\partial x_n} = 0 \tag{A5}$$

where the derivative of the transported variable ϕ normal to the boundary face is set to zero. The transported variable, ϕ at the boundary are extrapolated along the stream-wise direction of the fluid flow within the domain at each iteration. For a low volume fraction of dispersed phase (particles), the Lagrangian approach with one-way coupling was used, i.e. the airflow transports the particles, but the effect of particles movements on the flow was neglected. In this approach, the airflow field was first simulated, and then the trajectories of individual particles were evaluated using particle equation of motion. Trajectories of individual particles can be tracked by integrating a force balance equation on the particle. This force balance involves the particle inertia balanced by forces acting on the particles, and can be written as,

$$\frac{du_i^p}{dt} = F_D + F_g + F_i \tag{A6}$$

where F_g is the gravity term, which is defined as

$$F_g = \frac{g(\rho_p - \rho_g)}{\rho_p} \tag{A7}$$

and ρ_p and ρ_g denote the density of particle material and air, respectively. F_D is the drag force per unit particle mass, and F_i is an additional force (force/unit particle mass) term that is added accordingly. These last two terms are discussed in the sections to follow.

A.2. Micron particles

For micron particles, F_D is given by

$$F_D = \frac{18\mu_g}{\rho_p d_p^2}\frac{C_D \mathrm{Re}_p}{24}(u_g - u_p) \tag{A8}$$

where u_g and u_p are the gas (air) velocity and particle velocity, respectively. d_p is the particle volume equivalent diameter. μ_g is the molecular viscosity of the fluid and Re_p is the particle Reynolds number, which is defined as

$$\mathrm{Re}_p \equiv \frac{\rho_p d_p \left|u^p - u^g\right|}{\mu_g} \tag{A9}$$

The drag coefficient, C_D, can be taken from the following equation:

$$C_D = a_1 + \frac{a_2}{\mathrm{Re}} + \frac{a_3}{\mathrm{Re}^2} \tag{A10}$$

where a_1, a_2 and a_3 are constants that apply to smooth spherical particles over several ranges of Re given by Morsi and Alexander (1972). The additional force term F_i is neglected for micron particles.

A.3. Nanoparticles

For nanoparticles, a form of Stokes' drag law (Ounis et al., 1991) is available. In this case, F_D is defined as,

$$F_D = \frac{18\mu}{d_p^2 \rho_p C_c}(u_i^g - u_i^p) \tag{A11}$$

C_c is the Cunningham correction factor to Stokes' drag law, which can be calculated from,

$$C_c = 1 + \frac{2\lambda}{d_p}(1.257 + 0.4e^{-(1.1 d_p/2\lambda)}) \tag{A12}$$

where λ is the molecular mean free path.

The additional force term F_i is given for the nanoparticles and is defined as follows:

$$F_i = F_{Bi} + F_{Li} + F_{Ti} \tag{A13}$$

where F_{Bi} is the Brownian force term, F_{Li} is Saffman's lift force term and F_{Ti} is the thermophoretic force term. Amplitudes of the Brownian force components are of the form,

$$F_{Bi} = \zeta_i \sqrt{\frac{\pi S_0}{\Delta t}} \tag{A14}$$

where ζ_i is a zero mean, unit variance independent Gaussian random numbers. The components of the Brownian force, are modelled as a Gaussian white noise process with spectral intensity $S_{n,ij}$ given by Li and Ahmadi (1992):

$$S_{n,ij} = S_0 \delta_{ij} \tag{A15}$$

where δ_{ij} is the Kronecker delta function, and

$$S_0 = \frac{216\nu k_B T}{\pi^2 \rho d_p^5 (\rho_p/\rho)^2 C_c} \tag{A16}$$

T is the absolute temperature of the fluid, ν is the kinematic viscosity, and k_B is the Boltzmann constant.

The Saffman's lift force, or lift due to shear, is also included in the additional force term. The lift force used is from the work of Li and Ahmadi (1992) which is a generalization of the expression originally provided by Saffman (1965):

$$F_{Li} = \frac{2K\nu^{1/2}\rho d_{ij}}{\rho_\mathrm{p} d_\mathrm{p} (d_{lk} d_{kl})^{1/4}}(\vec{v} - \vec{v}_\mathrm{p}) \tag{A17}$$

K is a constant and is equal to 2.594 while d_{ij} is the deformation tensor. This form of the lift force is intended for small particle Reynolds numbers. Also, the particle Reynolds number based on the particle–fluid velocity difference must be smaller than the square root of the particle Reynolds number based on the shear field. Since this restriction is valid for submicron particles, it is recommended to use this option only for submicron particles.

Small particles suspended in a gas that has a temperature gradient experiences a thermophoretic force in the direction opposite to that of the gradient. This effect is included in the thermophoretic force term:

$$F_{Ti} = -D_{T,p}\frac{1}{m_p T}\frac{\partial T}{\partial i} \tag{A18}$$

where $D_{T,p}$ is the thermophoretic coefficient. We use the form suggested by Talbot et al. (1980):

$$F_{Ti} = -\frac{6\pi d_p \mu^2 C_s (K + C_t Kn)}{\rho(1 + 3C_m Kn)(1 + 2K + 2C_t Kn)} \frac{1}{m_p T} \frac{\partial T}{\partial i} \quad \text{(A19)}$$

where $Kn = 2\lambda/d_p$, $K = k/k_p$ and $k = (15/4)\mu R$. Kn is Knudsen number, λ is mean free path of the fluid, k is fluid thermal conductivity based on translational energy only, k_p is particle thermal conductivity, m_p is the particle mass, T is the local fluid temperature and μ is fluid viscosity. The values of the constants are $C_s = 1.17$, $C_t = 2.18$, $C_m = 1.14$. This expression assumes that the particle is a sphere and that the fluid is an ideal gas.

References

Chang, H.K., 1989. In: Chang, H.K., Paiva, M. (Eds.), Flow Dynamics in the Respiratory Tract. Respiratory Physiology an Analytical Approach. Dekker, New York.

Cheng, K.H., Cheng, Y.S., Yeh, H.C., Guilmette, A., Simpson, S.Q., Yang, Y.H., Swift, D.L., 1996. In-vivo measurements of nasal airway dimensions and ultrafine aerosol deposition in the human nasal and oral airways. J. Aerosol Sci. 27 (5), 785–801.

Cheng, Y.S., Yamada, Y., Yeh, H.C., Swift, D.L., 1988. Diffusional deposition of ultrafine aerosols in a human nasal cast. J. Aerosol Sci. 19 (6), 741–751.

Dai, Y.T., Juang, Y.J., WU, Y.Y., Breysse, Y.Y., Hsu, D.J., 2006. In vivo measurements of inhalability of ultralarge aerosol particles in calm air by humans. J. Aerosol Sci. (37), 967–973.

Hahn, I., Scherer, P.W., Mozell, M.M., 1993. Velocity profiles measured for airflow through a large-scale model of the human nasal cavity. J. Appl. Physiol. 75 (5), 2273–2287.

Harrington, J.B., Metzger, K., 1963. Ragweed pollen density. Am. J. Bot. 50, 532–539.

Häußermann, S., Bailey, A.G., Bailey, M.R., Etherington, G., Youngman, M.J., 2001. The influence of breathing patterns on particle deposition in a nasal replicate cast. J. Aerosol Sci. 33, 923–933.

Isabey, D., Chang, H.K., 1981. Steady and unsteady pressure-flow relationships in central airways. J. Appl. Physiol. 51, 1338–1348.

Kelly, J.T., Prasad, A.K., Wexler, A.S., 2000. Detailed flow patterns in the nasal cavity. J. Appl. Physiol. 89, 323–337.

Kelly, J.T., Asgharian, B., Kimbell, J., Wong, B.A., 2004. Particle deposition in human nasal airway replicas manufactured by different methods. Part I: Inertial regime particles. Aerosol Sci. Technol. 38, 1036–1071.

Kesavanathan, J., Swift, D.L., 1998. Human nasal passage particle deposition: the effect of particle size, flow rate and anatomical factors. Aerosol Sci. Technol. 28, 457–463.

Keyhani, K., Scherer, P.W., Mozell, M.M., 1995. Numerical simulation of airflow in the human nasal cavity. J. Biomech. Eng. 117, 429–441.

Li, A., Ahmadi, G., 1992. Dispersion and deposition of spherical particles from point sources in a turbulent channel flow. Aerosol Sci. Technol. 16, 209–226.

Morsi, S.A., Alexander, A.J., 1972. An investigation of particle trajectories in two-phase flow systems. J. Fluid Mech. 55 (2), 193–208.

Ounis, H., Ahmadi, G., McLaughlin, J.B., 1991. Brownian diffusion of submicrometer particles in the viscous sublayer. J. Colloids Interf. Sci. 143 (1), 266–277.

Saffman, P.G., 1965. The lift on a small sphere in a slow shear flow. J. Fluid Mech. 22, 385–400.

Shi, H., Kleinstreuer, C., Zhang, Z., 2006. Laminar airflow and nanoparticle or vapor deposition in a human nasal cavity model. J. Biomech. Eng. 128, 697–706.

Shi, H., Kleinstreuer, C., Zhang, Z., 2007. Modeling of inertial particle transport and deposition in human nasal cavities with wall roughness. J. Aerosol Sci. 38, 391–419.

Sullivan, K.J., Chang, H.K., 1991. Steady and oscillatory trans-nasal pressure-flow relationships in healthy adults. J. Appl. Physiol. 71, 983–992.

Swift, D.L., Proctor, D.F., 1977. In: Brain, J.D., Proctor, D.F., Reid, L.M. (Eds.), Access of Air to the Respiratory Tract. Respiratory Defence Mechanisms. Marcel Dekker, New York, NY.

Swift, D.L., Montassier, N., Hopke, P.H., Karpen-Hayes, K., Cheng, Y.S., Su, Y.F., Yeh, H.C., Strong, J.C., 1992. Inspiratory deposition of ultrafine particles in human nasal replicate cast. J. Aerosol Sci. 23 (1), 65–72.

Swift, D.L., Strong, J.C., 1996. Nasal deposition of ultrafine218 Po Aerosols in human subjects. J. Aerosol Sci. 27 (7), 1125–1132.

Talbot, L., Cheng, R.K., Schefer, R.W., Willis, D.R., 1980. Thermophoresis of particles in a heated boundary layer. J. Fluid Mech. 101 (4), 737–758.

Weinhold, I., Mlyynski, G., 2004. Numerical simulation of airflow in the human nose. Eur. Arch. Otorhinolaryngol. 261, 452–455.

Wen, J., Inthavong, K., Tu, J.Y., Wang, S.M., 2008. Numerical simulations for detailed air flow dynamics in a human nasal cavity. Respir. Physiol. Neurobiol. 161, 125–135.

Yu, G., Zhang, Z., Lessman, R., 1998. Fluid flow and particle deposition in the human upper respiratory system. Aerosol Sci. Technol. 28, 146–158.

Zamankhan, P., Ahmadi, G., Wang, Z., Hopke, P.H., Cheng, Y.S., Su, W.C., Leonard, D., 2006. Airflow and deposition of nanoparticles in a human nasal cavity. Aerosol Sci. Technol. 40, 463–476.

Zhang, Z., Kleinstreuer, C., Donohue, J.F., Kim, C.S., 2005. Comparison of micro- and nano-size particle depositions in a human upper airway model. J. Aerosol Sci. 36, 211–233.